Disturbed flow in a patient-specific arteriovenous fistula for hemodialysis: Multidirectional and reciprocating near-wall flow patterns

Bogdan Ene-Iordache [a,*], Cristina Semperboni [b], Gabriele Dubini [c], Andrea Remuzzi [a,d]

[a] *IRCCS – Istituto di Ricerche Farmacologiche "Mario Negri", Ranica, BG, Italy*
[b] *Department of Biomedical Engineering, Politecnico di Milano, Milano, MI, Italy*
[c] *Laboratory of Biological Structure Mechanics – LaBS, Department of Chemistry, Materials and Chemical Engineering "Giulio Natta", Politecnico di Milano, Milano, MI, Italy*
[d] *Department of Management, Information and Production Engineering, University of Bergamo, Dalmine, BG, Italy*

1. Introduction

A well-functioning vascular access (VA) serves as lifeline for the patients on hemodialysis. There is general consensus in the literature on the superiority of autogenous arteriovenous fistulae (AVF) over arteriovenous grafts (AVG) and central venous catheters regarding VA survival, related complications and costs (Leermakers et al., 2013; Vassalotti et al., 2012). Despite the existence of clinical guidelines (NKF/KDOQI, 2006) recommending well-defined criteria to create AVF, a high failure rate has been reported due to the formation of juxta-anastomotic stenoses. In studies performed between 1977 and

* Correspondence to: Laboratory of Biomedical Technologies, Clinical Research Center for Rare Diseases Aldo e Cele Daccò, Via G.B. Camozzi 3, 24020 Ranica, BG, Italy. Tel.: +39 035 4535390; fax: +39 035 4535371.

E-mail address: bogdan.ene-iordache@marionegri.it (B. Ene-Iordache).

2002 where VA was provided by AVF (Allon and Robbin, 2002), the mean early failure rate was 25% (range 2–53%) while the mean one-year patency rate was 70% (42–90%).

Since the 1990s computational fluid dynamics (CFD) applied to blood vessels was intensively used to assess the wall shear stress (WSS) in the study of the link between hemodynamics and cardio-vascular disease. Beside characterization of the general flow field, many patient-specific CFD studies have focused on the assessment of the so-called "disturbed flow" acting near wall. The pattern of dis-turbed flow is irregular, it features secondary and recirculation eddies that may change in direction with time and space, and hence it exerts low and oscillating WSS on the endothelial layer (Davies, 2009). Localization of atherosclerosis within specific sites in branch points or curvatures of the arterial tree, in humans and in experimental animals (Chiu and Chien, 2011), led to the concept that the distur bed flow is related to the vascular lesions. Also in VA, recent findings

about the localization of these sites matching areas of disturbed flow (Remuzzi and Ene-Iordache, 2013) may add new insights into the mechanism of pathogenesis of neointimal hyperplasia (NH) after the surgical creation of the anastomosis.

By using CFD we have shown that disturbed flow may develop in focal sites of radial-cephalic models of AVF, either in *side-to-end* or *end-to-end* configuration, at least in idealized geometry with flow conditions resembling the initial days after surgery (Ene-Iordache and Remuzzi, 2012). In that study, we speculated on a local remo-deling mechanism for the neointima formation induced by the local disturbed flow. The present study was aimed at investigating whether disturbed flow occurs also in a patient-specific AVF model, which would confirm the above hypothesis on the hemodynamics-related mechanism of local development of stenosis.

2. Materials and methods

2.1. Patient-specific data and AVF model

The subject was a 48 year old male, who participated in a prospective clinical trial (Caroli et al., 2013). As per the study protocol (Bode et al., 2011), the patient had blood sample, ultrasound (US) and magnetic resonance angiography (MRA)
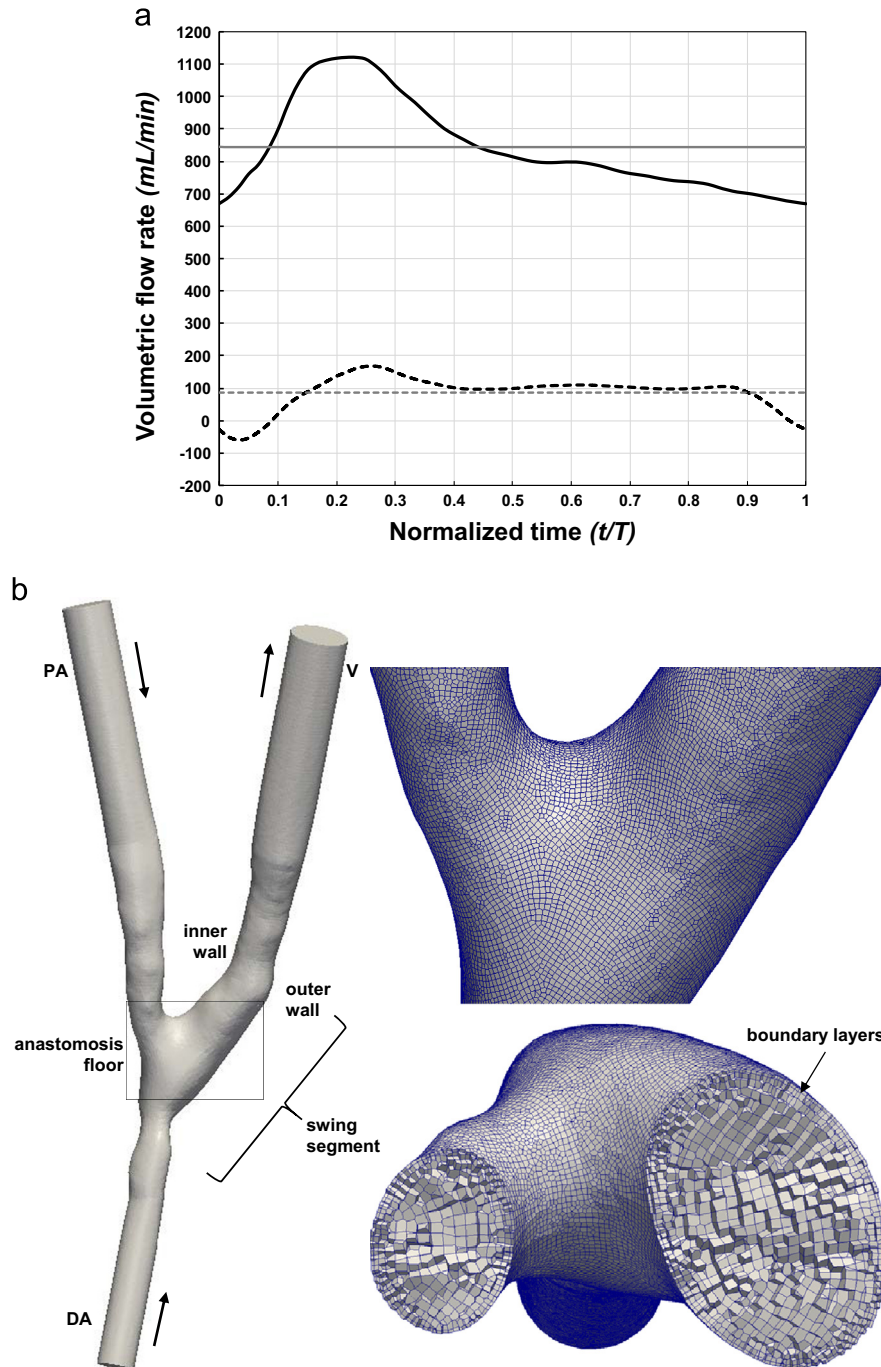

Fig. 1. (a) Patient-specific blood volumetric flow rate waveforms derived from US pulsed-Doppler velocity spectra images. Continuous and dashed curves represent the blood flow in the PA and DA, respectively. Blood flow in the DA changes direction during the cardiac cycle, negative is antegrade (towards the hand) and positive is retrograde flow. Horizontal lines indicate the time-averaged blood flow rate over the cardiac cycle, 844 mL/min for PA and 86.5 mL/min for DA, respectively. (b) 3-D surface of the model and detail of the surface and volume meshwork showing internal cells and the boundary layers near the wall. PA, proximal artery; DA, distal artery. Arrows indicate the main direction of blood flow.

investigations of the left arm vessels, pre-operatively and after six weeks post-operatively. Patient-specific flow rate waveforms derived from US in the arteries, namely the proximal artery (PA) and the distal artery (DA) are shown in Fig. 1a. Details on their calculation and about the 3D reconstruction of the AVF model are provided in the Supplementary material on-line.

Since hexahedral meshes are known to reduce the computational costs with respect to the tetrahedral ones (De Santis et al., 2011), and to provide higher accuracy in the calculation of WSS (De Santis et al., 2010), we decided to use hexahedral cells for the AVF mesh. The internal volume was discretized with the *foamyHexMesh* mesher which is part of *OpenFOAM* v. 2.3.1 suite (OpenFOAM Team, 2014). Starting from the surface geometry, this mesher produced high quality hexahedral grids with regular shape cells. Two thin boundary layers of cells were generated near the wall in order to increase the accuracy of WSS calculation. A coarser mesh with more than 128,000 cells, and two refined, consisting of more than 300,000 and 780,000 cells were generated for the AVF model. After a steady CFD study for mesh-independence, which yielded a maximum difference in WSS lower than 5% relative to the finest grid, we concluded that the mesh with 300,000 cells resolves accurately the flow field and related WSS inside this type of AVF setting. Full and detailed view of the AVF grid, with the highlighted anastomosis floor and the swing segment (SS) of cephalic vein, is presented in Fig. 1b.

2.2. CFD simulation of blood flow in the AVF

Transient flow simulation was performed using the *OpenFOAM* code, a multi-purpose and well validated CFD tool based on the finite volume method (OpenFOAM Team, 2014). We considered blood non-Newtonian (Supplementary material) and assumed density 1.05 g/cm^3.

As boundary conditions we prescribed blood flow rates at the PA and DA inlets with the waveforms shown in Fig. 1a, traction-free at the vein outlet and no-slip at the walls. We used *pimpleFoam*, a transient solver for incompressible flows using the PIMPLE (merged PISO-SIMPLE) algorithm and first order Euler time integration scheme. This solver adjusts the time step based on a user-defined maximum Courant–Friedrichs–Lewy (CFL) number, which we set to 1. The numerical simulation ran in 19,940 variable time steps for a cycle, corresponding to a temporal resolution between 0.018 and 0.067 ms, and results were saved for post-processing in 1000 equal time steps for each cycle. Three complete cardiac cycles were solved in order to damp the initial transients of the fluid and only the results of the third cycle were considered for data processing.

For the PA and DA inlets, and the vein outlet, we calculated the Reynolds and the Womersley numbers as described previously (Ene-Iordache and Remuzzi, 2012). Geometric and hemodynamic features of the patient-specific AVF model are summarized in Table 1.

2.3. Data post-processing

We localized reciprocating disturbed flow by means of the oscillatory shear index (OSI) (He and Ku, 1996) and multidirectional disturbed flow by means of the transverse WSS (transWSS) metric (Peiffer et al., 2013). Also, aimed at describing the nature of the hemodynamic shear, we generated plots of WSS magnitude in time in several feature points on the AVF surface. General flow field, WSS patterns, and a video clip showing the evolution of WSS vectors throughout one cardiac cycle are provided as Supplementary material.

3. Results

The patterns of disturbed flow in this patient-specific AVF are presented in Fig. 2. Reciprocating shear disturbed flow zones revealed by high OSI (Fig. 2a), are located on the inner wall of the SS, after the vein curvature, and on the DA near the anastomosis floor. Multidirectional flow, as characterized by medium-to-high transWSS (>10 dyne/cm^2, Fig. 2b) is located on the anastomosis floor, the whole SS and, in a lesser extent more distally, after the

vein curvature. Such patterns of transWSS indicate that shear vectors change direction throughout the cardiac cycle on the whole SS surface, while they remain approximately parallel to the main direction of flow on the PA and DA walls.

The time-course of the WSS vector throughout the pulse cycle for four feature points on the AVF surface is presented in Fig. 3 while their near-wall flow characteristics are summarized in Table 2. These points are shown in Fig. 2a and were selected specifically to char-acterize the shear vector acting on the inner wall of PA (P1) corre-sponding to laminar bulk flow, matching the highest OSI on the DA and SS (P2 and P3) in disturbed flow zones, and on the outer wall of the vein (P4) after the SS curvature. The graphs reveal high WSS on the PA (P1, time-averaged 78.9 dyne/cm^2), specific for laminar and high blood flow. Pure reciprocating flow develops on the DA, oscil-lating with the frequency of heart rate and having a low average (P2, OSI 0.42, and time-averaged WSS 0.7 dyne/cm^2). High frequency, either multidirectional or reciprocating flow develops on the inner wall of the SS (P3, transWSS 22.7 dyne/cm^2, OSI 0.47 and time-averaged 2.1 dyne/cm^2). More distally on the outer vein, the WSS pattern is multidirectionally lowered (P4, transWSS 6.1 dyne/cm^2) and oscillating with high frequency around a big value (time-aver-aged 66.7 dyne/cm^2). The evolution of the WSS vectors throughout the cardiac cycle in the featured points above can be well observed in the Supplemental video clip.

Supplementary material related to this article can be found online.

4. Discussion

While the mechanism of vessel wall pathophysiology has been the subject of considerable research, the idea of the link between disturbed flow and NH in VA is relatively new (Remuzzi and Ene-Iordache, 2013). In the present study we employed image-based CFD in a realistic model of side-to-end radial-cephalic AVF, showing development of disturbed flow. The working hypothesis regarding existence of disturbed flow zones that may trigger the local remodeling mechanism (Ene-Iordache and Remuzzi, 2012), was corroborated also in this patient-specific AVF case. Our study is in agreement with previous idealized geometry (Ene-Iordache et al., 2013; Niemann et al., 2010) and image-based CFD studies (He et al., 2013) that reported development of reciprocating dis-turbed flow (high OSI) on the AVF walls.

This is the first study to reveal the multi-directionality of WSS on the anastomosis floor and on the SS walls. The high values of transWSS in Fig. 2b are indicative for development of complex vortices that rotate also the shear stress vectors on the vessel wall. At the same time, in some areas of the inner wall of the SS, reci-procating disturbed flow develops as shown in Fig. 2a. Another novel finding was to show that the nature of reciprocating flow developed on DA and SS walls is different. While the DA experi-enced pure reciprocating flow at the frequency of the heart rate, the oscillations of the WSS on the SS wall were at high frequencies, induced by the turbulent bulk flow at this level.

Table 1
Geometric and hemodynamic features of the patient-specific AVF model.

	Diameter (mm)	Volumetric flow rate (mL/min)	Re	Wo
PA inlet	5	844 (1121; 669)	1387 (1879; 1080)	3.91 (3.95; 3.88)
DA inlet	3.8	86 (168; −60)	161 (338; 106)	2.76 (2.87; 2.69)
V outlet	5.9	930 (1283; 639)	1263 (1788; 837)	4.52 (4.58; 4.44)

Note: Waveforms of the flow rate in the PA and DA are shown in Fig. 1. The flow rate in V is obtained by their summation. *Re* and *Wo* numbers are calculated for the given diameters and expressed as time-averaged and (maximum; minimum) values over the pulse cycle.
PA, proximal (radial) artery; DA, distal (radial) artery; V, (cephalic) vein; *Re*, Reynolds number; *Wo*, Womersley number.
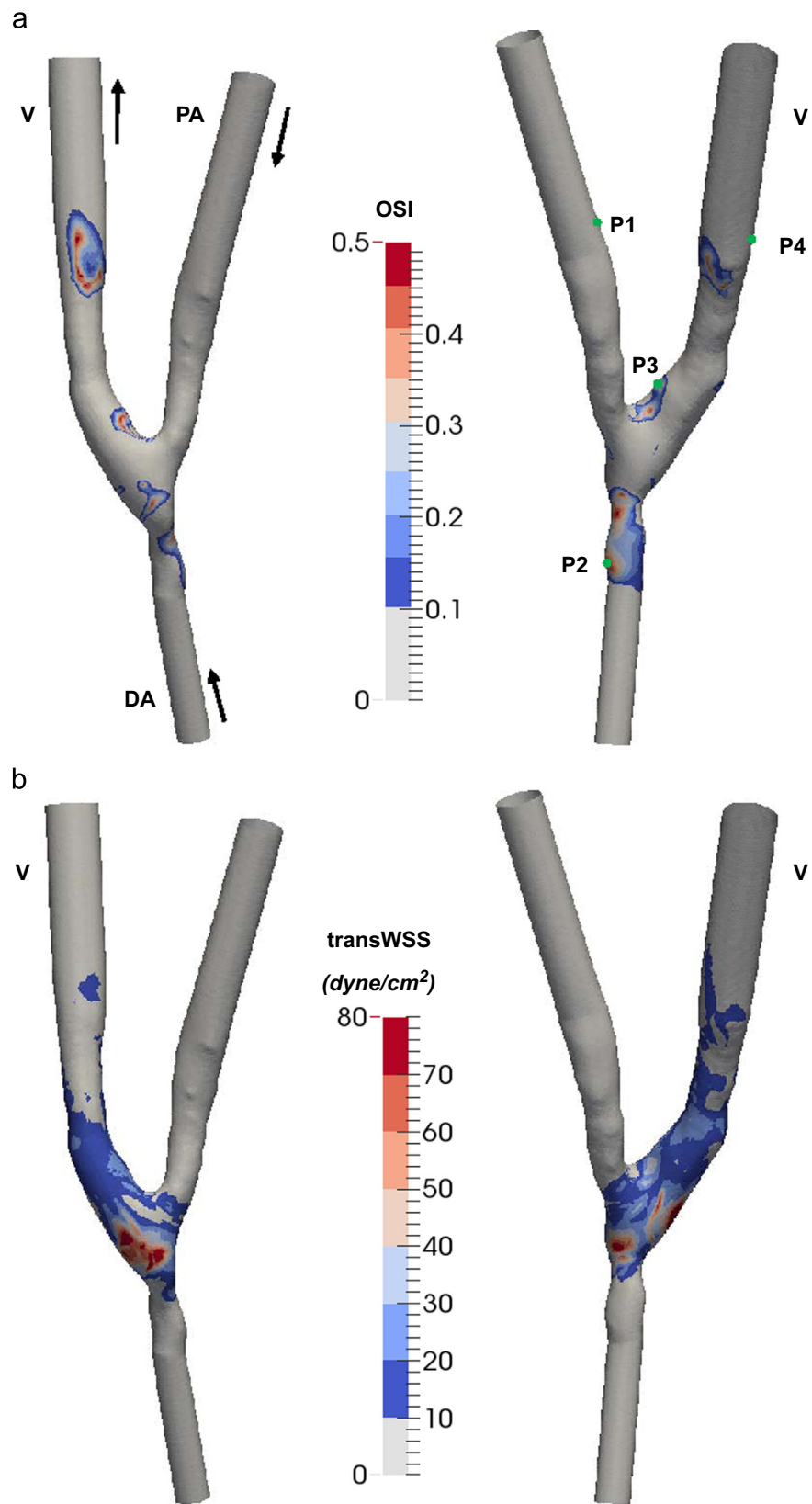
Fig. 2. Distribution of hemodynamic wall parameters on the AVF wall: (a) plot of OSI; (b) plot of tranWSS. Values of OSI between 0 and 0.1 and of transWSS below 10 dyne/cm² were represented in light grey to emphasize the pattern of disturbed flow on the AVF surface. Left, front view; right, rear view of the AVF.

Our results are confirmed by an in vivo study in canines (Jia et al., 2015) showing that NH develops more on the inner com-pared to the outer wall of SS, and compared with the proximal vein. Also, in a clinical study (Marie et al., 2014), serial AVF patients were showing development of turbulence only in the SS, while spiral laminar flow developed in the PA and distally in the draining vein. By solving the numerical solution with a very high temporal resolution we could catch the transition from laminar to turbulent
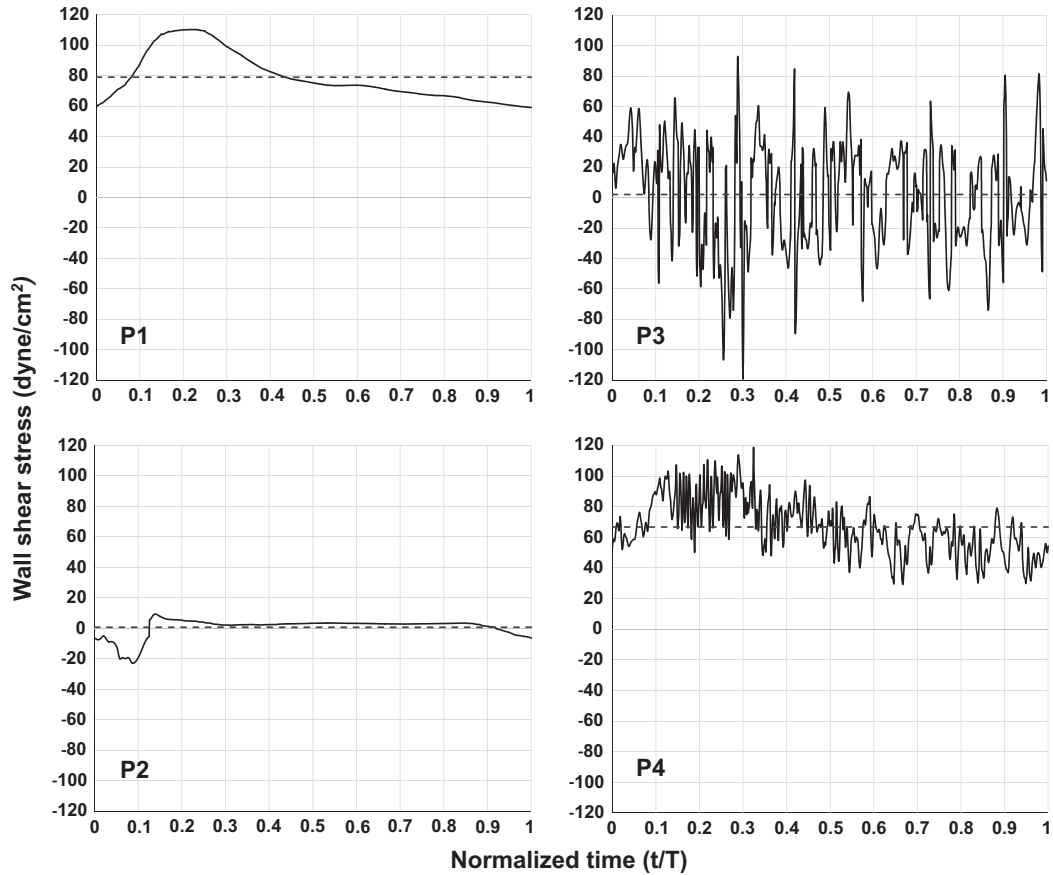
Table 2
Characteristics of near-wall flow at four feature points on the AVF surface.

Point	Position	Type of bulk flow	TKE (cm^2/s^2)	Type of disturbed flow	OSI	TransWSS ($dyne/cm^2$)	Max WSS ($dyne/cm^2$)	Min WSS ($dyne/cm^2$)	TAWSS ($dyne/cm^2$)
P1	PA (inner wall)	Laminar	89.2	–	0	0.7	110.2	59.0	78.9
P2	DA	Laminar	37.1	Reciprocating	0.42	1.2	9.4	−23.0	0.7
P3	SS (inner wall)	Turbulent	270.1	Reciprocating, multidirectional	0.47	22.7	92.4	−119.2	2.1
P4	V (outer wall)	Turbulent (damped)	203.9	Multidirectional	0.003	6.1	118.7	29.3	66.7

Note: The position of the four feature points is as shown in Fig. 2a (right).
PA, proximal (radial) artery; DA, distal (radial) artery; SS, swing segment; V, vein (cephalic); OSI, oscillatory shear index; WSS, wall shear stress; transWSS, transverse WSS; TAWSS, time-averaged WSS; TKE, turbulent kinetic energy (see Supplementary material on-line).

flow that develops in the SS, in line with similar findings of other authors (Lee et al., 2007; McGah et al., 2013).

Our study has obvious implications for elucidating the hemodynamic forces involved in the initiation of venous wall thickening in VA. The high frequency shear oscillations on the SS wall, having a low time-averaged WSS, may trigger or enhance venous NH. A similar conclusion was achieved by Himburg and Friedman (2006), showing that regions of porcine iliac arteries with increased endothelial permeability experience higher frequency oscillations in shear. While there is considerable evidence in vitro on laminar pulsatile vs. oscillatory shear, demonstrating clearly the atherogenic effect of pure reciprocating flow on the endothelium (Chiu

and Chien, 2011), few data exist in literature on the effect of multidirectional WSS.

Among the limits of the work, the study of only one patient-specific model with no longitudinal data is recognized, recalling the need of further larger studies. We also did not include the compliance of the wall in the AVF model. McGah et al. (2014) studied the effects of wall distensibility, finding lower time-averaged WSS compared to the rigid-walled simulation in a side-to-end AVF, but whether this affects also the near-wall disturbed flow should be further investigated. However, the technologies available today allow to optimize anastomotic geometries (Walsh et al., 2003) or to conduct longitudinal patient-specific studies for the

follow-up of VA adaptation and local remodeling (He et al., 2013; Sigovan et al., 2013).

In conclusion, in the present study we have studied the local patterns of WSS in a patient-specific side-to-end anastomosis, an AVF setting with high blood flow developed at six weeks post-opera-tively. We have found that the swing segment of the vein is a conduit subjected to multidirectional hemodynamic shear stress and simul-taneously develops reciprocating disturbed flow in some focal points. This combination may boost the initiation of NH after the surgically creation of the AVF, leading to subsequent failure of VA.

Conflict of interest

All the authors certify that they have NO affiliations with or involvement in any organization or entity with any financial interest (such as honoraria; educational grants; participation in speakers' bureaus; membership, employment, consultancies, stock ownership, or other equity interest; and expert testimony or patent-licensing arrangements), or non-financial interest (such as personal or pro-fessional relationships, affiliations, knowledge or beliefs) in the sub-ject matter or materials discussed in this manuscript.

Acknowledgments

Appendix A. Supplementary materials

Supplementary data associated with this article can be found in the online.

References

Allon, M., Robbin, M.L., 2002. Increasing arteriovenous fistulas in hemodialysis patients: problems and solutions. Kidney Int. 62, 1109–1124.

Bode, A., Caroli, A., Huberts, W., Planken, N., Antiga, L., Bosboom, M., Remuzzi, A., Tordoir, J., 2011. Clinical study protocol for the ARCH project-computational modeling for improvement of outcome after vascular access creation. J. Vasc. Access 12, 369–376.

Caroli, A., Manini, S., Antiga, L., Passera, K., Ene-Iordache, B., Rota, S., Remuzzi, G., Bode, A., Leermakers, J., van de Vosse, F.N., Vanholder, R., Malovrh, M., Tordoir, J., Remuzzi, A., 2013. Validation of a patient-specific hemodynamic computational model for surgical planning of vascular access in hemodialysis patients. Kidney Int. 84, 1237–1245.

Chiu, J.J., Chien, S., 2011. Effects of disturbed flow on vascular endothelium: pathophysiological basis and clinical perspectives. Physiol. Rev. 91, 327–387.

Davies, P.F., 2009. Hemodynamic shear stress and the endothelium in cardiovas-cular pathophysiology. Nat. Clin. Pract. Cardiovasc. Med. 6, 16–26.

De Santis, G., De Beule, M., Van Canneyt, K., Segers, P., Verdonck, P., Verhegghe, B., 2011. Full-hexahedral structured meshing for image-based computational vascular modeling. Med. Eng. Phys. 33, 1318–1325.

De Santis, G., Mortier, P., De Beule, M., Segers, P., Verdonck, P., Verhegghe, B., 2010. Patient-specific computational fluid dynamics: structured mesh generation from coronary angiography. Med. Biol. Eng. Comput. 48, 371–380.

Ene-Iordache, B., Cattaneo, L., Dubini, G., Remuzzi, A., 2013. Effect of anastomosis angle on the localization of disturbed flow in 'side-to-end' fistulae for hae-modialysis access. Nephrol. Dial. Transplant. 28, 997–1005.

Ene-Iordache, B., Remuzzi, A., 2012. Disturbed flow in radial-cephalic arteriovenous fistulae for haemodialysis: low and oscillating shear stress locates the sites of stenosis. Nephrol. Dial. Transplant. 27, 358–368.

He, X., Ku, D.N., 1996. Pulsatile flow in the human left coronary artery bifurcation: average conditions. J. Biomech. Eng. 118, 74–82.

He, Y., Terry, C.M., Nguyen, C., Berceli, S.A., Shiu, Y.T., Cheung, A.K., 2013. Serial analysis of lumen geometry and hemodynamics in human arteriovenous fistula for hemodialysis using magnetic resonance imaging and computational fluid dynamics. J. Biomech. 46, 165–169.

Himburg, H.A., Friedman, M.H., 2006. Correspondence of low mean shear and high harmonic content in the porcine iliac arteries. J. Biomech. Eng. 128, 852–856. Jia, L., Wang, L., Wei, F., Yu, H., Dong, H., Wang, B., Lu, Z., Sun, G., Chen, H., Meng, J., Li, B., Zhang, R., Bi, X., Wang, Z., Pang, H., Jiang, A., 2015. Effects of wall shear stress in venous neointimal hyperplasia of arteriovenous fistulae. Nephrology 20, 335–342.

Lee, S.W., Smith, D.S., Loth, F., Fischer, P.F., Bassiouny, H.S., 2007. Importance of flow division on transition to turbulence within an arteriovenous graft. J. Biomech. 40, 981–992.

Leermakers, J.J., Bode, A.S., Vaidya, A., van der Sande, F.M., Evers, S.M., Tordoir, J.H., 2013. Cost-effectiveness of vascular access for haemodialysis: arteriovenous fistulas versus arteriovenous grafts. Eur. J. Vasc. Endovasc. Surg. 45, 84–92. Marie, Y., Guy, A., Tullett, K., Krishnan, H., Jones, R.G., Inston, N.G., 2014. Patterns of blood flow as a predictor of maturation of arteriovenous fistula for haemo-dialysis. J. Vasc. Access 15, 169–174.

McGah, P.M., Leotta, D.F., Beach, K.W., Aliseda, A., 2014. Effects of wall distensibility in hemodynamic simulations of an arteriovenous fistula. Biomech. Model. Mechanobiol. 13, 679–695.

McGah, P.M., Leotta, D.F., Beach, K.W., Eugene Zierler, R., Aliseda, A., 2013. Incom-plete restoration of homeostatic shear stress within arteriovenous fistulae. J. Biomech. Eng. 135 (1), 011005.

Niemann, A.K., Udesen, J., Thrysoe, S., Nygaard, J.V., Frund, E.T., Petersen, S.E., Hasenkam, J.M., 2010. Can sites prone to flow induced vascular complications in a-v fistulas be assessed using computational fluid dynamics. J. Biomech. 43, 2002–2009.

NKF/KDOQI, 2006. Clinical Practice Guidelines for Vascular Access.

Peiffer, V., Sherwin, S.J., Weinberg, P.D., 2013. Computation in the rabbit aorta of a new metric-the transverse wall shear stress-to quantify the multidirectional character of disturbed blood flow. J. Biomech. 46, 2651–2658.

Remuzzi, A., Ene-Iordache, B., 2013. Novel paradigms for dialysis vascular access: upstream hemodynamics and vascular remodeling in dialysis access stenosis. Clin. J. Am. Soc. Nephrol. 8 (12), 2186–2193.

Sigovan, M., Rayz, V., Gasper, W., Alley, H.F., Owens, C.D., Saloner, D., 2013. Vascular remodeling in autogenous arterio-venous fistulas by MRI and CFD. Ann. Biomed. Eng. 41, 657–668.

OpenFOAM Team, 2014. The OpenFOAM Foundation. ⟨http://www.openfoam.org⟩.

Vassalotti, J.A., Jennings, W.C., Beathard, G.A., Neumann, M., Caponi, S., Fox, C.H., Spergel, L.M., 2012. Fistula first breakthrough initiative community education. Semin. Dial. 25, 303–310.

Walsh, M.T., Kavanagh, E.G., O'Brien, T., Grace, P.A., McGloughlin, T., 2003. On the existence of an optimum end-to-side junctional geometry in peripheral bypass surgery—a computer generated study. Eur. J. Vasc. Endovasc. Surg. 26, 649–656.